Monolithically Integrated Active Components: A Quantum-Well Intermixing Approach

Erik J. Skogen, *Member, IEEE*, James W. Raring, *Student Member, IEEE*, Gordon B. Morrison, *Member, IEEE*, Chad S. Wang, Vikrant Lal, *Student Member, IEEE*, Milan L. Mašanović, *Student Member, IEEE*, and Larry A. Coldren, *Fellow, IEEE*

Invited Paper

***Abstract*—As the demand for bandwidth increases, the communications industry is faced with a paradigm shift. Photonic integration is a key technology that will facilitate this shift. Monolithic integration allows for the realization of highly functional optical components, called photonic integrated circuits. Herein, we discuss the advantages and potential applications of photonic integration, and after a brief overview of various integration techniques, provide a detailed look at our work using a novel quantum well intermixing processing platform.**

***Index Terms*—Ion implantation, laser tuning, semiconductor lasers, wavelength division multiplexing (WDM).**

I. Introduction

MONOLITHIC integration of optoelectronic components is the key to realizing low-cost, high-functionality devices that have the capability to revolutionize the communications industry. Although not a new concept, monolithic integration of various optical functions now appears to be feasible, and perhaps the only way to truly revitalize the optical component industry. With today's technology, the generation, detection, modulation, switching, and transport of light on chip enables cost reduction, but it will also allow for a new generation of high functionality photonic integrated circuits (PICs) with reduced size and power dissipation.

Of course, monolithic integration has already occurred in the electronics industry, allowing the once discrete transistor, resistor, and capacitor to reside on the same chip, the electronic integrated circuit (IC). The advent of the IC allowed for electronic devices to be smaller and cheaper than their discrete counterparts, and most importantly, gave rise to a set of high functionality ICs that discrete components could not emulate. The field of optoelectronics faces a similar shift from discrete to integrated components, where the concepts and potential payoffs are similar to that in the electronics industry, yet the monolithic integration of optoelectronic components cannot be compared so simply to that of electronic devices.

Currently, the majority of optoelectronic components in use in the field are of a discrete nature. That is, each component is designed to perform one specific task. In practice, several components with differing functions are then interconnected, typically via fiber splices, in order to achieve the desired operation. This method has one advantage in that each component is optimized for one specific function, enabling that device to perform its task flawlessly. However, there are several shortcomings involved with this method of system construction. One is the difficulty in coupling light on and off each discrete chip. Advances in the coupling between the semiconductor chip and a fiber optic cable using mode converters is a significant step in reducing the coupling loss, yet it is still a dominant source of optical loss. Another is the expense involved with the discrete packaging of each component. The packaging of optoelectronic devices is the major cost source for the component.

A reduction of the packaging cost can be accomplished by using a method called copackaging. Copackaging involves the integration of discrete optoelectronic chips within the same package. Each component is still fabricated discretely and is designed for one specific task. However, the coupling problem continues to exist, although it is device-to-device not device-to-fiber.

A. Benefits of Photonic Integration

The monolithic integration of the optoelectronic devices on the same chip offers the potential to completely eliminate the device-to-device coupling problem. This can provide a significant reduction in packaging cost and package size as well as increased reliability and reduced power dissipation. Increased reliability results from the elimination of possible mechanical movements amongst the elements of an optical train and the reduced driving currents allowed by the reduction in optical coupling loss between elements. The power dissipation is reduced for this same reason. Furthermore, the potential for high functionality components such as widely tunable transmitters and chip scale wavelength conversion devices will open new avenues for wavelength division multiplexing (WDM) applications such as dynamic provisioning, reconfigurable optical

Manuscript received September 30, 2004; revised February 1, 2005.

E. J. Skogen was with the Department of Electrical and Computer Engineering, University of California, Santa Barbara, CA 93106 USA. He is now with Sandia National Laboratories, Albuquerque, NM 87123 USA (e-mail: ejskoge@sandia.gov).

J. W. Raring, G. B. Morrison, C. S. Wang, V. Lai, M. L. Mašanović, and L. A. Coldren are with the Department of Electrical and Computer Engineering, University of California, Santa Barbara, CA 93106 USA.

Digital Object Identifier 10.1109/JSTQE.2005.846525

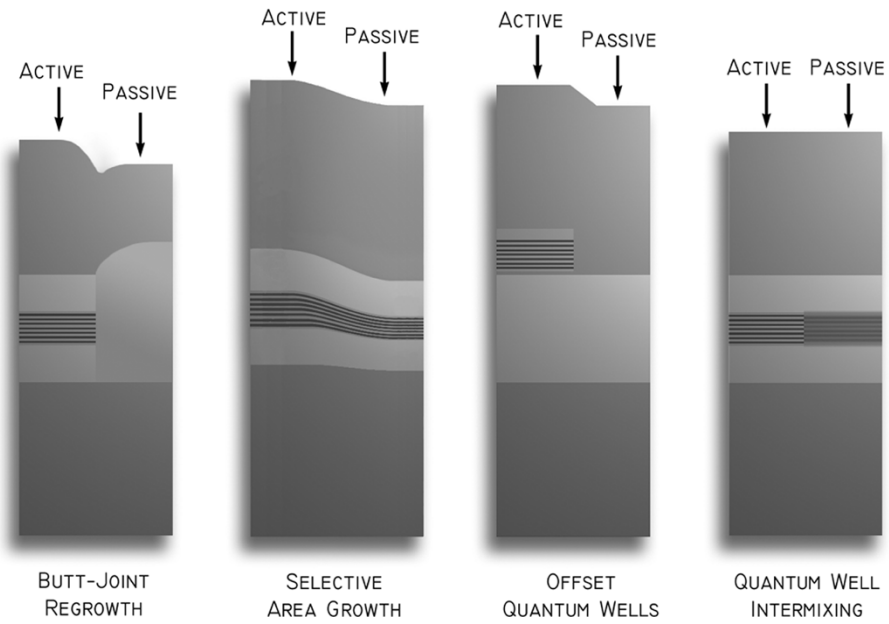

Fig. 1. Various techniques for achieving active and passive sections orthogonal to the growth direction.

add/drop multiplexers (ROADMs), wavelength routing, and optical packet switching.

The potential drawback, however, is the fact that each component must now be fabricated on the same chip, and to do so is technologically difficult. Compromises in device performance or increases in fabrication complexity must be avoided or at least minimized. There are several techniques that have been used in the past, such as the use of offset quantum wells, butt-joint regrowth, selective area growth (SAG) and quantum-well intermixing (QWI) to enable numerous components to be formed on the same chip with a common fabrication process. However, before trying to evaluate the advantages of these approaches, we will review the requirements and present some general guidelines for monolithic integration.

B. Guidelines for Photonic Integration

There are some general requirements that must be fulfilled when monolithically integrating optoelectronic components. First, each integrated component must function as intended. The performance of each integrated device does not necessarily have to meet the performance characteristics of a discrete component, but must still operate in a way that is suitable for the operation of the circuit as a whole. The second requirement states that the operation of one device must not adversely effect the operation of another. This stems from the fact that each component in an integrated circuit, whether it be electronic or optoelectronic, should be isolated from the other components on chip and function as if it were a discrete component. These requirements allow for the design of PICs using optoelectronic building blocks, that is, discrete components that share a common growth and processing platform that can be arranged in such a way that a more complex device or PIC can be obtained.

There are also a few general guidelines to bear in mind when implementing a method for monolithic integration. First, the method used should not be prohibitively time consuming or expensive. This is the key to realizing the cost reduction over existing discrete components. Second, the integration should not lead to device compromises. This is a difficult task due to the fact that each discrete device was designed with a single function in mind and, therefore, the device structure evolved on an individual basis. However, as stated earlier, the integrated component must only perform as intended, it does not necessarily need to match the performance of a discrete device. This affords some flexibility in the design of the device in terms of the device structure, possibly allowing devices with differing functionalities to be fabricated using the same growth and processing platform. Lastly, the process complexity should remain constant as the number of integrated components increases. An additional processing step or the substitution of one step for one that is more complex can increase the manufacturing cost and, in the case of complex processing/growth can lead to yield reduction. A review of some of the integration methods used in the past are given in the following section.

II. Integration Background

There has been some great success in producing simple PICs based on various methods. As illustrated in Fig. 1, such methods include, but are not limited to, a butt-joint regrowth technique [1], selective area growth (SAG) methods [2], the use of an offset quantum-well active region [3], and QWI [4]–[7]. The first, butt-joint regrowth involves the selective removal of waveguide core material followed by the regrowth of an alternate waveguide core using different material composition. This process is inherently difficult involving a precise etch of the original waveguide core, followed by a regrowth of waveguide material with composition and thickness variables.

Another process, the SAG process, involves the selective growth using a mask. In this process, a mask is patterned on the surface of the wafer prior to epitaxial growth. The geometry of the mask has a role in determining the growth near the vicinity

of the mask and can be used to obtain different compositions and thickness across the wafer. This method is useful in fabricating several quantum-well band edges across the wafer, but due to the fact that the thickness is inherently coupled with the band edge in these regions, the optical confinement factor cannot be independently optimized.

The use of offset quantum wells, where the quantum wells are grown above the waveguide and selectively removed in various regions post-growth, has been used with great success in fabricating various integrated structures, sampled-grating distributed Bragg reflector (SG-DBR) lasers with integrated electro-absorption modulators (EAMs) [8], SG-DBR lasers with integrated semiconductor optical amplifiers (SOAs) [9], SG-DBR lasers with integrated Mach-Zehnder modulators [10], optical receivers, and wavelength converters. The drawback of the offset quantum-well method, however, is the limitation of each integrated component to one of two band edges, not allowing for the flexibility necessary for the fabrication of complex, high-performance PICs.

QWI has been used in the past to fabricate a multitude of devices. There are a great deal of techniques that have evolved over the years to accomplish selective intermixing, such as impurity-induced disordering (IID) [11], impurity-free vacancy-enhanced disordering (IFVD) [12], photoabsorption-induced disordering (PAID) [13], and implantation-enhanced interdiffusion [14] to name just a few.

QWI makes use of the metastable nature of the compositional gradient found at heterointerfaces. The natural tendency for materials to interdiffuse is the basis for the intermixing process. The rate at which this process takes place can be enhanced with the introduction of a catalyst. Using a lithographically definable catalyst patterning process, the QWI process can be made selective. This is the process by which virtually all selective QWI is performed, whether it is by the introduction of impurities or by the creation of vacancies.

We have developed a method to further control the QWI process, to achieve any number of quantum-well band edges in the structure. The method is based on the selective removal of the catalyst. This process fits ideally with the suggested guidelines for monolithic integration. It is not prohibitively time consuming or expensive, it is versatile enough that is does not lead to device compromises, and the process complexity remains simple such as not to increase cost or decrease yield. Using this method we have fabricated short-cavity DBR lasers with integrated modulators, widely-tunable multisection SG-DBR lasers with integrated modulators, and chip-scale wavelength converters.

The various QWI techniques all benefit from their relative simplicity; however the flexibility of each is not equal. For example, the IID technique commonly uses dopants as the impurity to accelerate intermixing. This can have a detrimental effect on the electrical nature of the device. Another example involves the method that the technique is applied. For instance, the IFVD and implantation enhanced intermixing techniques can be applied to full device structures or partially grown epitaxial base structures. Asserting that there are several methods by which QWI can be applied, the degree of desired flexibility determines the combination of technique and method used.

III. Method for Integration

As described earlier, a technique that offers great potential for large scale monolithic integration is QWI. A unique QWI processing platform was developed to fulfill the requirements and guidelines for monolithic integration. In the following section, the QWI processing platform is described, the process details given, and the characterization methods and results will be presented.

A. QWI Processing Platform

In this paper, we employ the implant-enhanced interdiffusion technique, which relies on the diffusion of point defects created during an ion implantation. This method has also been shown to have good spatial resolution, and be controllable using anneal time, temperature, and implant dose [14]. Wide ranges of implant energies have been used in this process from the mega-electronvolt range down to tens of kiloelectronvolts. Commonly, these implants are performed on full lasers structures, where the vacancies are created in the upper cladding, and must diffuse long distances before reaching the quantum wells. Although this is not detrimental to the intermixing itself, the device performance may be hindered due to the redistribution of dopants which control the electrical nature of the device. This can be avoided by using a partially grown laser structure with a sacrificial cap layer, which can be subsequently removed, and the upper cladding regrown as described in [15]. While [15] demonstrated such a concept, the process was not optimized, as multiple implant and anneal cycles were required to achieve significant intermixing.

The implant dose can be used to control the extent of intermixing using a single anneal step [7]. Such an effect would allow the formation of several band edges across the wafer, which is useful for the monolithic integration of several optoelectronic components. However, to achieve three band edges, two ion implants are required. With the majority of ion implants being farmed out to specialty houses, the task can be time consuming and expensive. Furthermore, each additional desired band edge requires an additional ion implant, a process that begins to show limitations.

The QWI method developed in this paper uses the selective removal of the vacancies created during the ion implant to effectively halt the intermixing process at the desired level. This method requires a single ion implant followed by a rapid thermal anneal. The extent of intermixing can be controlled using the anneal time. Once the desired band edge is reached, the anneal is stopped and the vacancies are removed in that region. The anneal is then continued until the desired band edge is reached another section, at which point the vacancies are removed in this section. As will be shown, this process can be repeated to achieve any number of band edges across the wafer.

B. QWI Process Details

The epitaxial base structure was designed, not only to perform intermixing experiments, but also to facilitate the fabrication of DBR based lasers. In this respect, the base structure was designed with multiple stop etch layers to allow access to the high

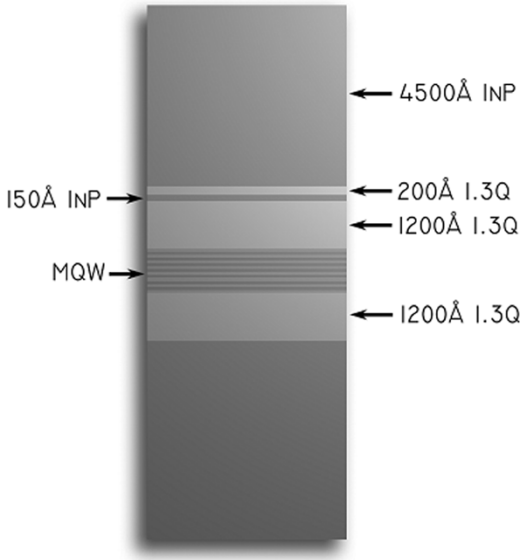

Fig. 2. Epitaxial base structure with both seven or ten quantum-well active region and 4500 Å InP implant buffer layer.

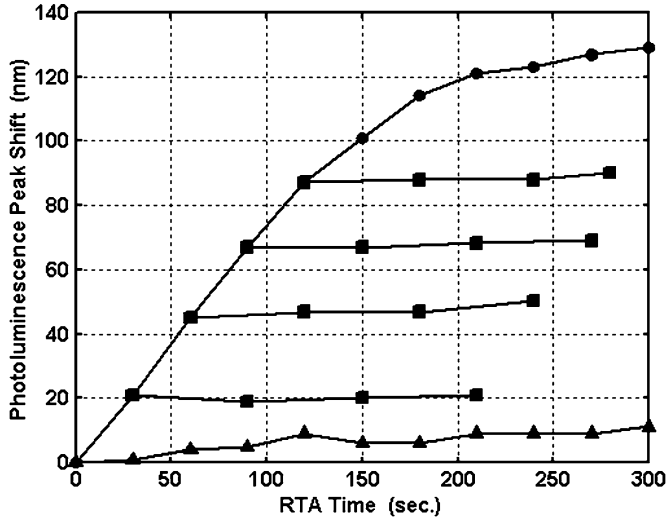

Fig. 3. Peak photoluminescence peak shift as a function of anneal time, showing the initial linear increase in the peak shift and the complete halting of the peak shift for samples for which the implant buffer layer has been etched. Symbols indicate nonimplanted (triangles), implanted (circles), and samples with partial anneal followed by the removal of the implant buffer layer (squares).

field region of the optical mode, which allows for the formation of the high index contrast gratings used in the DBR mirrors.

The base structure, shown in Fig. 2, was grown on a sulfur doped InP wafer using a Thomas Swan horizontal flow rotating-disc metal-organic chemical vapor deposition (MOCVD) reactor. The base structure consists of seven 6.5-nm quantum wells, eight 8.0-nm barriers, sandwiched between 120-nm-thick 1.3Q (InGaAsP $\lambda_g = 1.3$ μm) layers, making up the waveguide layer. The MQW active region was designed to have an emission wavelength of 1560 nm. Above the waveguide, a 15-nm InP stop etch layer, and a 20-nm 1.3Q stop etch layer was followed by a 450-nm InP layer. The top most InP layer, herein called the implant buffer layer, was designed to capture a low energy ion implant, thereby creating vacancies far from the MQW active region.

The base structure was subjected to an ion implant using P^+ at an energy of 100 keV, yielding a range of 90 nm, with a dose of 5E14 cm^{-2}. The substrate temperature during the implant was held at 200 °C to aid in point defect(s) formation [5].

The unique intermixing process was investigated using several samples cleaved from an implanted base structure, as described in the previous section. These samples were annealed at 675 °C for various times ranging from 30 to 300 s at 30-s intervals and the extent of the intermixing was measured by room-temperature photoluminescence. As the point defect(s) front moves through the quantum-well region, the blue-shift increases linearly. Once the point defect(s) front has moved through the quantum-well region the blue-shifting ceases. This saturation of the blue-shift can be observed above 120 nm ,as shown in Fig. 3. After the 30-, 60-, 90-, 120-s anneals, the implant buffer layer was removed from the respective samples. These samples were then subjected to additional anneal cycles. We found that removing the implant buffer layer halted the blue-shift during these anneals. The arrest of the blue-shift is the result of the removal of the abundance of vacancies, necessary for intermixing, along with the implant buffer layer. With this process, it is possible to achieve any number of band edges across the wafer, limited only by the practical number of lithographic process steps [16].

C. QWI Characterization

In order to characterize the intermixed quantum-well material, several experiments have been performed to investigate properties and extract parameters that have implications for PICs. The modal loss of the QWI material is an important parameter in the design of PICs. It is shown in the following section that the waveguide modal loss of QWI material is inversely proportional to the extent of intermixing. Another important aspect of the intermixed quantum wells has to do with the quantum confined Stark effect (QCSE). We have observed a strong exciton peak in the intermixed quantum wells; we also show for the first time the shift of the exciton peak as a function of reverse bias. We show that the QWI material is an ideal candidate for negative chirp parameter electroabsorption modulators by relating the change in absorption to the change in refractive index through the Kramers–Kronig relation.

Using active/passive devices, where the passive region is composed of intermixed quantum wells, the modal loss can be extracted. This is done by plotting the differential efficiency of the active/passive device as a function of passive region length. The passive waveguide loss was measured for several sets of devices each with a different magnitude of photoluminescence shift. The modal loss of the structure is dependent on the configuration of the waveguide; the modal loss is dependent on the optical mode overlap with sources of loss. In this experiment, active/passive buried ridge stripe (BRS) Fabry–Perot (FP) laser devices were tested under pulsed conditions, initially with a passive waveguide length of 2500 μm, cleaved back in steps of 500 μm. The active/passive laser differential efficiency was extracted from laser light versus current measurements, assuming equal reflectivity for the front and back facet. Once

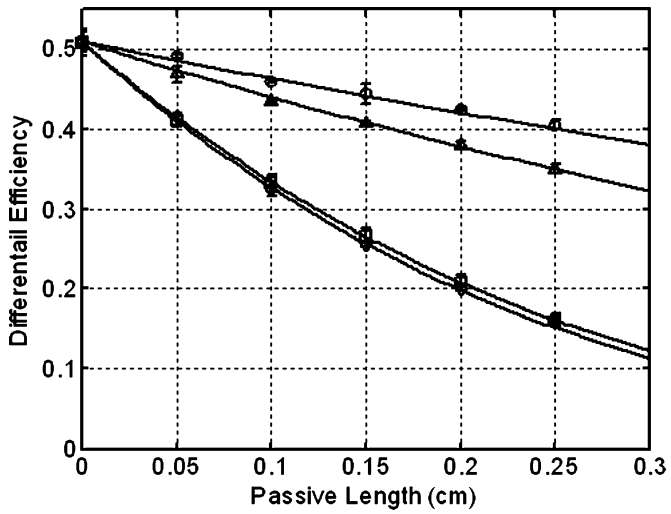

Fig. 4. Differential efficiency of active/passive lasers as a function of passive region length. Symbols indicate data with passive region photoluminescence peaks at 1428 (circles), 1448 (triangles), 1485 (squares), and 1488 nm (diamonds). Solid lines are curve fits used for extracting passive region modal loss, 1.5 (circles), 2.3 (triangles), 6.4 (squares), and 6.7 cm^{-1} (diamonds).

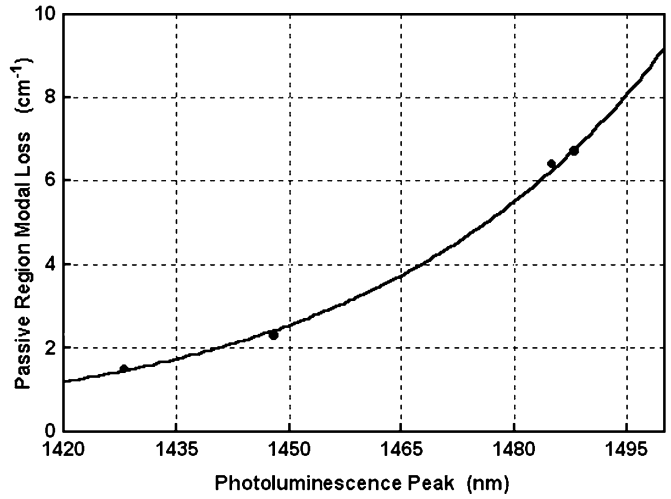

Fig. 5. Passive region modal loss as a function of photoluminescence peak wavelength. Solid line indicates an exponential curve fit, while symbols indicate modal loss data extracted from active/passive lasers.

the all-active BRS, FP lasers have been pulse tested and the laser characteristics extracted, the theoretical active/passive differential efficiency can be plotted as a function of passive region length and the modal loss computed [7]. Fig. 4 shows data and curve fits for several sets of active/passive devices each with a different magnitude of intermixing applied. The passive region loss was plotted as a function of photoluminescence peak wavelength, shown in Fig. 5. An exponential curve provides a good fit with the data. As evident from Fig. 5, the passive region modal loss is strongly dependent on the relative position of the intermixed band edge. The modal loss in the passive region can be minimized by maximizing the magnitude of intermixing.

It was implied that QWI material be used in the SG-DBR mirrors that are used to create the cavity of the widely-tunable SG-DBR laser. Here, intermixed quantum wells are used as the tuning medium, where quantized energy states remain. The

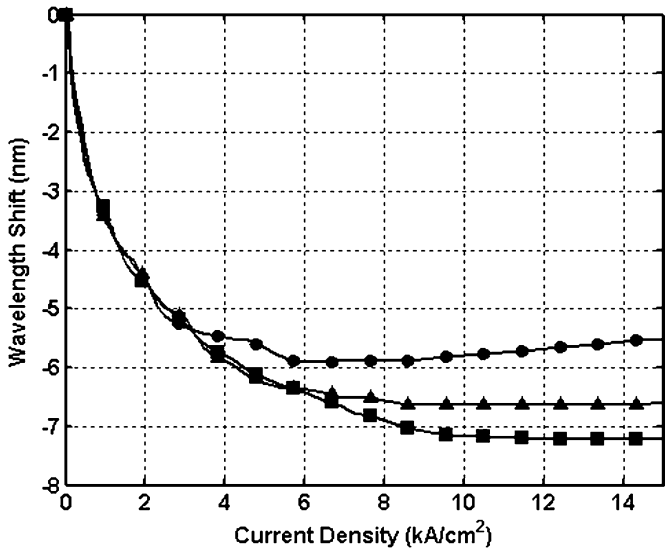

Fig. 6. Experimental tuning curve for samples with differing extents of intermixing. Symbols indicate wavelength shifts of 1475 (circles), 1446 (squares), and 1423 nm (triangles).

presence of quantized energy states allows the mirror to achieve a high tuning efficiency in a small volume of material. This is made possible by a more efficient band filling mechanism resulting from the step-function density of states [17].

The carrier induced refractive index change can be measured by biasing the gain region of an SG-DBR laser below threshold and observing the shift of the transmission notches as a function of injected current. Once the wavelength shift is found as a function of current injection, the wavelength shift can be translated to refractive index shift using the following:

$$\Delta \overline{n}_g = \overline{n}_g \cdot \frac{\Delta \lambda}{\lambda} \tag{1}$$

The variables in (1) indicate the change in modal group refractive index $\Delta \overline{n}_g$ the modal group index in the untuned waveguide $\overline{n}_g$ the change in wavelength $\Delta \lambda$ and the initial wavelength λ. We have previously shown that intermixed quantum wells provide sufficient refractive index shift by carrier injection to cover the full tuning range of the SG-DBR laser [16]. Fig. 6 shows the tuning results for three magnitudes of intermixed quantum wells.

Another simple tool for extracting material band edge absorption is photocurrent spectroscopy. The band edge absorption data can be exploited for design, optimization and performance-analysis of QWI integrated laser-modulators. We also present a detailed characterization of the evolution of band-edge absorption as a function of the degree of QWI in InGaAsP–based quantum wells. The ability to directly measure the QWI band edge, and to use this measurement for analysis of potential transmitter designs, will enable the engineering of superior, highly optimized integrated laser-modulator transmitters for telecommunications applications.

The photodiodes used in our photocurrent spectroscopy experiments are simple devices that can be rapidly fabricated for material characterization. The QWI process, as described earlier, is used to create three band edges on a single wafer—one as-grown and two intermixed. Each of the intermixed regions

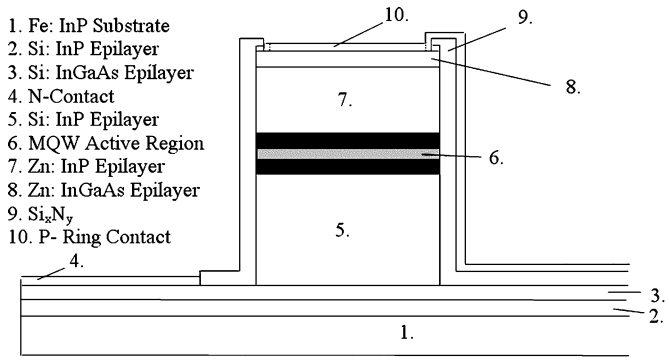

Fig. 7. Cross-sectional side view of a typical photodiode structure.

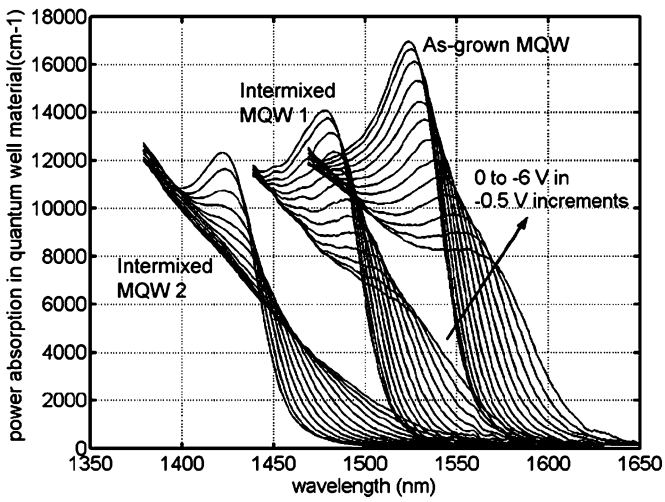

Fig. 8. Power absorption versus wavelength for as-grown and two regions whose quantum wells are intermixed to different levels.

are blue-shifted by a different amount. The three band edges are referred to quantitatively by the wavelengths, in nanometers, of their photoluminescence peaks.

Once each band edge was patterned, circular mesas ranging from 50 to 400 μm in radius were etched. The mesa etch is performed by reactive ion etching through the waveguide and into the n-type substrate. Some devices are grown on semi-insulating substrates, in which case reactive ion etching is used to remove the active region and waveguide, after which a wet etch is used to stop on the n contact InGaAs layer. A 2000-Å layer of SiNx is deposited by plasma-enhanced chemical vapor depostion (PECVD), and circular vias are patterned onto the mesas. Ti/Pt/Au ring contacts were deposited. The contacts are annealed at 410 °C for 30 s. Devices are wire bonded to AlN carriers. Fig. 7 shows a schematic of the simple photodiodes used in photocurrent spectroscopy experiments.

The photodiodes were characterized using a Varian Cary 500 spectrophotometer. A description of the test apparatus is given in [18]. Simple calculations are performed to extract an absorption coefficient from the photocurrent data. Measured incident power is reduced to account for reflection and p-contact absorption, and is converted to units of photons/s. Light incident to the photodiode surface is transverse-electric (TE) polarized. Transverse-magnetic (TM) light is not considered because in-plane laser devices operate with TE polarization. We have determined that back-scattered light is negligible due to scattering and absorption by the Ti/Pt/Au backside contact. The measured photocurrent is converted to electrons/second, and each electron is the result of one absorbed photon. Absorption is then obtained as

$$\alpha = \frac{-\ln\left(\frac{P_{\rm in}-P_{\rm out}}{P_{\rm in}}\right)}{L} \tag{2}$$

where $P_{\rm in}$ is the input power in photons per second, $\rm P_{out}$ is the output photocurrent in photons per second, and L is the total length of quantum-well material through which the light passes.

Fig. 8 shows representative band edge measurements obtained by photocurrent spectroscopy. The epitaxial material used for devices shown in Fig. 7 contained seven 65-Å compressively strained quantum wells and eight 80-Å barriers sandwiched between two 120-nm waveguides. The effect of QWI on the exciton peak is made clear by comparison of the band edges for the photodiodes fabricated from the as-grown MQW material versus those fabricated from intermixed MQW material. The diodes were biased from 0 to −6 V in −0.5 V increments. The band edges shown in Fig. 8 have photoluminescence peaks ($\lambda_{\rm pl}$) at 1537, 1483, and 1429 nm. As the degree of intermixing increases, and the exciton peaks shift to shorter wavelengths, the exciton magnitude decays significantly. With increased intermixing, the exciton peaks also decay more rapidly as a function of applied bias voltage.

The intermixing process results in group V atoms diffusing across the as-grown material boundaries, causing quantum wells to develop rounded edges, and become wider and shallower. This is consistent with the observed behavior of the exciton peaks, which are expected to decay more rapidly with applied voltage when the quantum wells are made shallower by QWI.

Absorption band edge data, such as that shown in Fig. 8, offer great potential for use in optimizing, analyzing, and understanding laser-EAM transmitters and photonic integrated circuits. Later in this paper, predictions of device performance are made using the absorption band edge data. These predictions are compared directly to the performance of actual laser-EAM transmitters. The predictions are shown to be in good agreement with the data.

IV. Integrated Devices

In this section, several of the active component integrated devices will be introduced and discussed. These devices make use of the QWI method discussed in the previous sections. Described herein are the short-cavity DBR laser with integrated electroabsorption modulator, the widely-tunable SG-DBR laser with integrated electroabsorption modulator, and two types of wavelength converter with on-chip widely-tunable continuous-wave laser source. In the past, there have been some analogous examples using one or more of the integration techniques described in Section II. For example, integrated DFB-EAMs have been very successful as commercial sources for moderate reach fiber links. These have used butt-joint [18] and SAG [19].

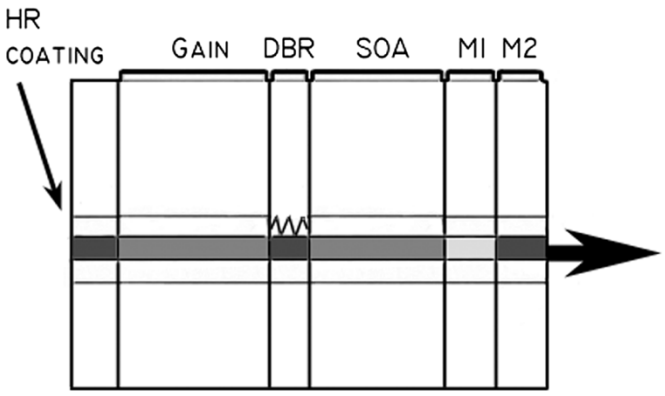

Fig. 9. Side-view schematic of the integrated short cavity DBR laser/EAM device.

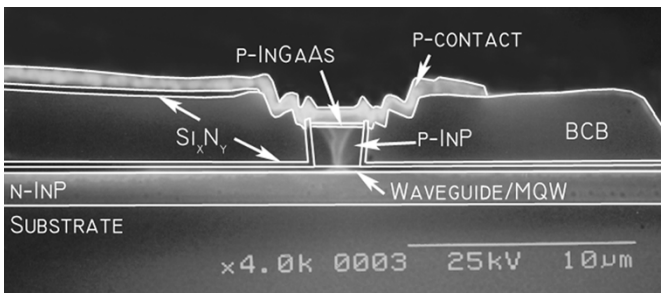

Fig. 10. End-on-view cross-sectional stain etch of the integrated short cavity DBR laser/EAM device.

A. Short Cavity DBR Laser With Integrated EAM

In designing a short-cavity DBR laser, considerations and tradeoffs have to be made regarding the mirror reflectivity, operating current, and temperature rise in the device. First, the cavity requires the length to be sufficiently short such that the mode spacing is wide enough on the DBR stopband to maintain single mode emission. With a high reflectivity (HR) back mirror, the front mirror needs to be optimized for low current operation in the laser at high powers ($>$10 mW). Here, we chose to design a short-cavity DBR laser with a HR coated back mirror, short gain section (150 μm), and a front DBR mirror (40 μm). The short front mirror is enabled by deep gratings resulting in a high coupling coefficient ($\kappa = 250$ cm^{-1}). This does not adversely affect the laser performance since it lies outside the gain region. A side-view schematic of the designed device is shown in Fig. 9, which, for demonstration, includes an integrated SOA and two-section EAM.

As described previously, a QWI processing platform was applied to optimize the band edge of each integrated device. For example, the gain and SOA sections were left at the as-grown band edge of $\lambda_{\rm pl} = 1540$ nm, the EAM was intermixed to $\lambda_{\rm pl} = 1500$ nm, and the DBRs and passive waveguides were further intermixed to $\lambda_{\rm pl} = 1430$ nm. The amount of intermixing for the EAM section was optimized by photocurrent spectroscopy for optimum extinction performance [20]. Following the top p-cladding regrowth, standard ridge lasers were fabricated [21]. To facilitate high-speed operation of the integrated EAM, benzocyclobutene (BCB) was patterned beneath the EAM contact metal for low pad capacitance. A cross section of the EAM is shown in Fig. 10.

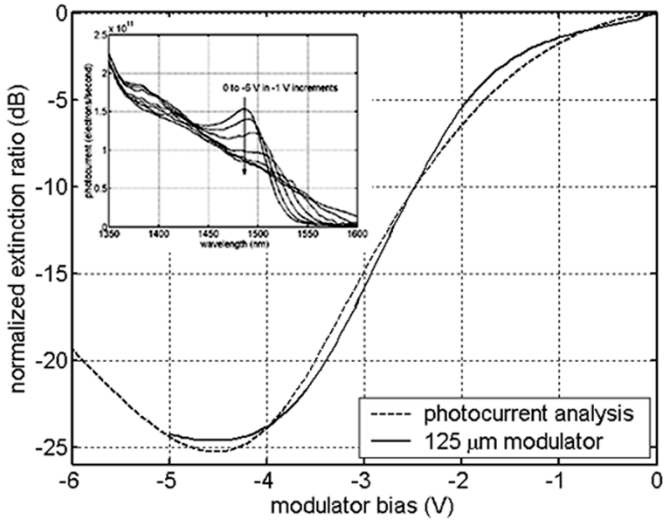

Fig. 11. DC extinction characteristic of a 125-μm integrated EAM computed with a simulation using photocurrent spectroscopy data from identical material. Inset shows photocurrent data used in extinction simulation.

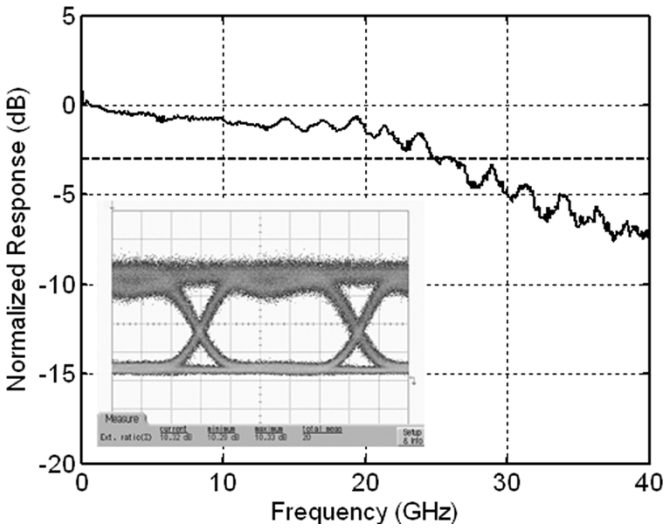

Fig. 12. Bandwidth of a 125-μm integrated EAM demonstrating 25 GHz. Inset is a 10-Gb/s eye diagram showing grater than 10-dB extinction with a 0.6-V swing.

The devices demonstrated good characteristics in terms of output power, efficiency, and side mode suppression ratio (SMSR) [22]. A threshold current of 7 mA was measured, and output powers greater than 10 mW were achieved with a gain section current of 30 mA [22].

The integrated EAM demonstrated greater than 20 dB optical extinction with $>$13-dB/V extinction efficiency for a 125 μm modulator, as shown in Fig. 11. The inset shows measured photocurrent spectroscopy data for this QWI material. This excellent performance is easily verified using absorption data taken by photocurrent spectroscopy from a similar device. Starting with a spline interpolation of absorption as a function of voltage, simple calculations, which account for optical overlap with the quantum wells and the effective index and length of the waveguide, lead to predicted DC extinction ratios for an EAM. In Fig. 11, the dotted line shows the simulated DC extinction of the 125-μm EAM at 1542 nm. Clearly, the photocurrent measurements allow reasonable estimation of

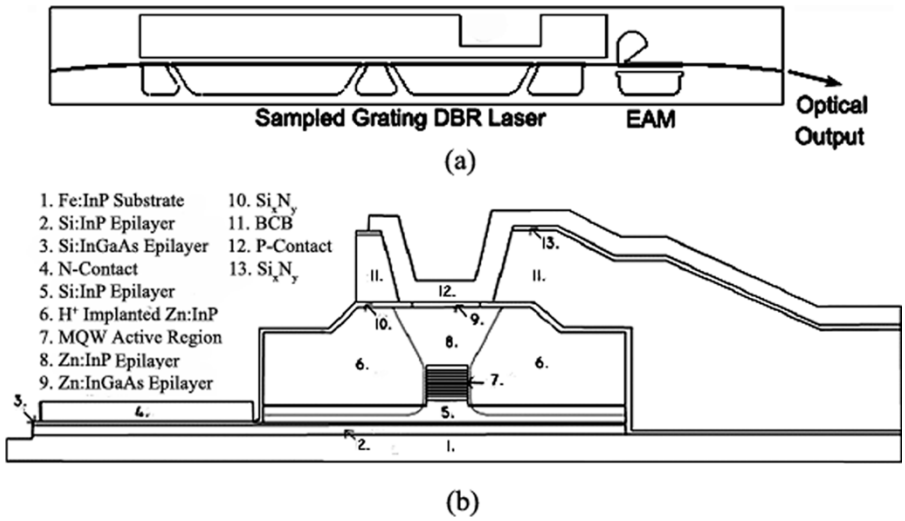

Fig. 13. (a) Top view schematic of the SG-DBR laser/EAM transmitters device architecture. (b) Cross-sectional schematic of modulator sections.

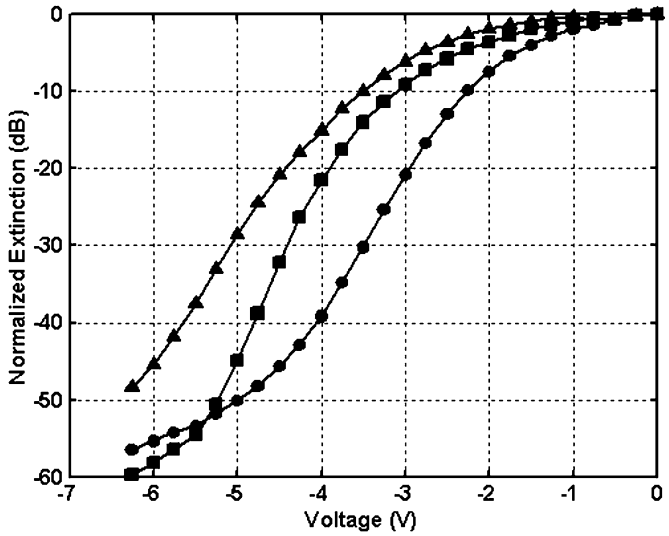

Fig. 14. DC extinction of a 175-μm modulator for wavelengths of 1558 (circles), 1570 (squares), and 1580 nm (triangles).

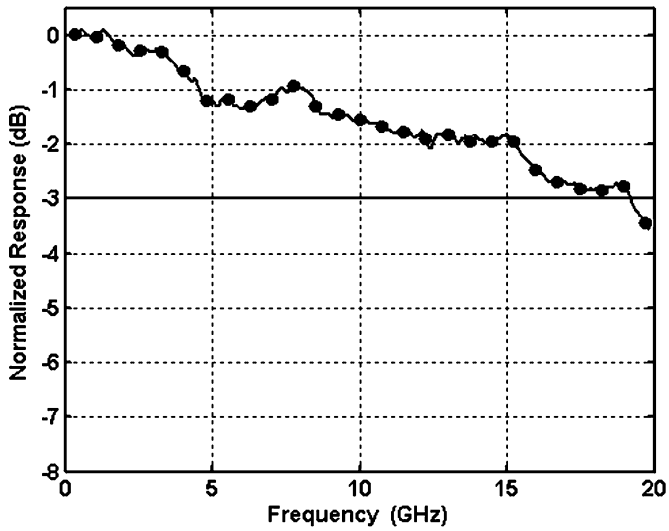

Fig. 15. Electrical to optical frequency response of a 175-μm modulator. The circular markers represent every 30th data point.

modulator performance. These results suggest that photocurrent spectroscopy can be used as a powerful tool for predicting device performance. The 3-dB modulation bandwidth was measured to be 25 GHz, as shown in Fig. 12. The inset shows open eye diagrams were achieved at 10 Gb/s with greater than 10-dB dynamic extinction at a DC bias of -3 V and a 0.6-V swing. From these data, it is clear that the QWI material in modulator sections can be controlled, and is of high optical and electrical quality.

B. SG-DBR Laser With Integrated EAM

Electroabsorption-modulated widely-tunable lasers are candidate sources for optical metropolitan area network applications, as they are compact and potentially low-cost. For efficient 10 Gb/s transmission, it is essential that the EAM demonstrate negative chirp behavior such that the dispersion penalty can be minimized. This characteristic may be achieved by exploiting the quantum confined stark effect (QCSE) with the use quantum wells as the EAM absorption medium.

The simple, robust QWI method described earlier provides an ideal integration platform for the fabrication of widely-tunable laser/QW-EAM transmitters. The ability to define multiple precisely tuned band-edges across a single chip, allows for the independent optimization of the EAM and passive components. The band-edge of the EAM can be blue-shifted such that it maintains a high absorption coefficient, reasonable insertion loss, and without severe degradation to the exciton peak. The passive component band-edge can be further blue-shifted for minimum loss. With the use of QWI, we have for the first time, fabricated a widely-tunable transmitter demonstrating negative chirp characteristics at 10 Gb/s over its entire tuning range.

The transmitter device, shown in Fig. 13, consists of a five section widely tunable SG-DBR laser followed by an EAM. The five sections of the SG-DBR laser are, from rear facet to front facet: 1) backside absorber; 2) rear mirror; 3) phase; 4) gain; and 5) front mirror. The phase and mirror sections function to

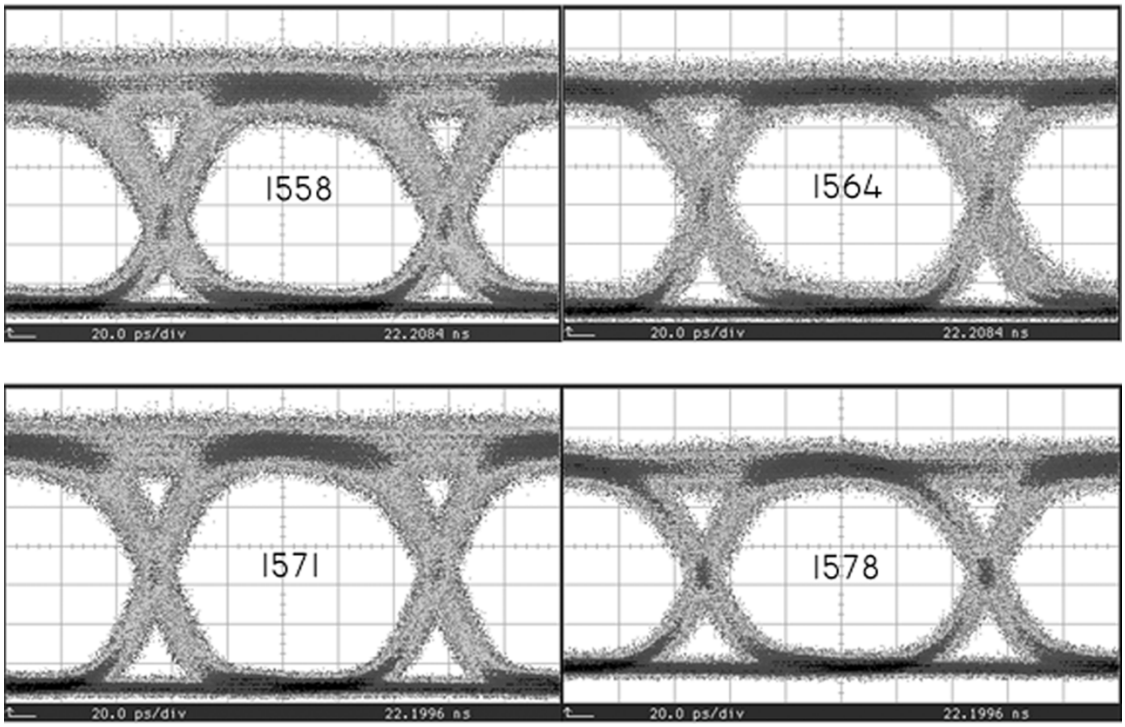

Fig. 16. 10-Gb/s back-to-back eye diagrams from transmitter at wavelengths of 1558, 1564, 1571, and 1578 nm.

tune the wavelength of the laser [7]. The lithographically defined mirrors make the SG-DBR laser ideal for monolithic integration due to the fact that no facets are required for operation. The process of these devices is described elsewhere [23].

The SG-DBR laser demonstrated a threshold current of 13 mA, with an output power of 10 mW at a gain section current of 100 mA. At this operating point, a side mode suppression ratio (SMSR) greater than 35 dB was achieved.

The EAM (175 μm) demonstrated over 40 dB of dc extinction for wavelengths of 1558, 1570, and 1580 nm, with efficiencies greater than 20 dB/V, as shown in Fig. 14. The efficient extinction properties are due to the combination of the centered quantum-well design and the intermixing process that allows for precise placement of the modulator band edge. The 3-dB bandwidth, shown in Fig. 15, of the same modulator was greater than 19 GHz. Eye diagrams, shown in Fig. 16, were taken at wavelengths of 1558, 1564, 1571, and 1578 nm with dc biases ranging from -2.1 to -3.8 V and peak-to-peak voltage swings ranging from 2.2 V to 3.4 V. Greater than 10-dB extinction was achieved at all wavelengths.

Transmission experiments at 10 Gb/s were performed using a nonreturn to zero (NRZ) pseudorandom-bit-sequence (PRBS) of $2^{31}-1$. A booster erbium doped fiber amplifier (EDFA) was used to launch the signal through Corning SMF-28 fiber. A variable optical attenuator was used to regulate the optical power into a optical receiver. Bit-error rate (BER) curves through 25, 50, and 75 km of fiber at a wavelength of 1564 nm are shown in Fig. 17. The EAM was biased at -3.5 V with a 2.0-V peak to peak swing. Error-free operation was achieved through 75 km of fiber with a power penalty of less than 0.5 dB. The shaping of the eye diagrams due to dispersion is clearly seen in the insets of Fig. 17 where the optical eye diagrams are shown after transmission through fiber. The noise performance for transmission through 75 km is limited by the signal attenuation of the fiber and the noise of the oscilloscope optical receiver.

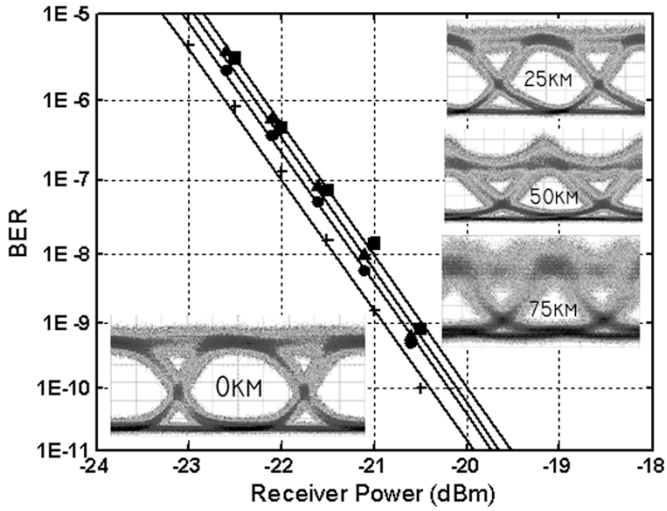

Fig. 17. BER curves and respective eye diagrams for back-to-back (cross), and transmission through 25 (circles), 50 (triangles), and 75 km (squares) of fiber at a wavelength of 1564 nm.

The low dispersion penalty for 10-Gb/s transmission demonstrated in Fig. 17 is indicative of negative chirp characteristics. In order to verify the chirp behavior of the modulator, the large signal chirp parameter was measured on the EAM and analysis was performed on the photocurrent data similar to that shown in Fig. 8 obtained from identical material as the transmitters. With the photocurrent data, differences in absorption between the band edge at 0 V and the band edges at each of the reverse biases are easily obtained. Application of the Kramers–Kronig transform to the absorption data, as described in [24], yields the index change as a function of voltage change.

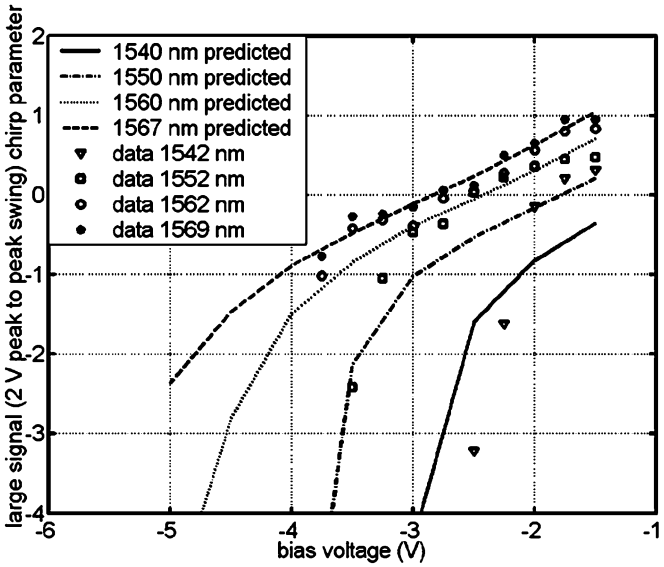

Fig. 18. Data points show measured large signal chirp as a function of bias voltage at 1542, 1552, 1562, and 1569 nm. Lines show predicted chirps at 1540, 1550, 1560, and 1567 nm.

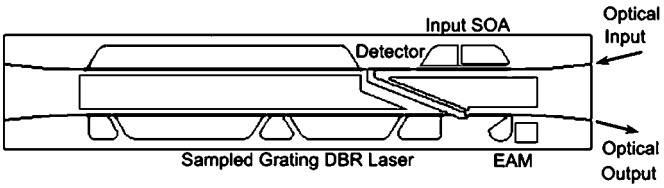

Fig. 19. (a) Top-view schematic of the OEIC wavelength converter architecture with the receiver ridge (upper) and transmitter ridge (lower).

With knowledge of index change as a function of voltage, and absorption change as a function of chirp, the large signal chirp can be calculated [25]. Fig. 18 compares the large signal chirp, as calculated from photocurrent spectroscopy, at wavelengths of 1540, 1550, 1560, and 1567 nm, with the chirp measured in the buried-ridge modulators at wavelengths of 1542, 1552, 1562, and 1569 nm. The 2-nm difference in wavelengths has been included to account for the fact that the photocurrent diodes were intermixed to $\lambda_{\rm pl} \approx 1508$ nm, whereas the transmitter EAMs were intermixed to $\lambda_{\rm pl} \approx 1510$ nm. Chirp measurements were made on the transmitters using Agilent's Time Resolved Chirp (TRC) software coupled with the required Agilent 86 146B optical spectrum analyzer. The measured dynamic chirp parameter, and the chirp parameter that is calculated directly from photocurrent spectroscopy, are in reasonable agreement. Clearly, the wavelength-agile negative chirp performance of the transmitters can be directly attributed to the band edge that is found in the QWI material from which the EAMs are fabricated. The QWI process that was used to shift the band edge in the EAM section of the device did not significantly detract from the exciton confinement. We, therefore, assert that QWI is a promising fabrication platform for implementation of high performance, widely tunable, negative chirp, 10-Gb/s laser-EAM transmitter devices.

C. Wavelength Converters

The integration of an optical receiver with a widely-tunable transmitter can provide wavelength conversion functionality, making applications such as wavelength routing and ROADMs possible. Using the same QWI integration platform as the laser/EAM transmitter, wavelength converters were fabricated. The device architecture, shown in Fig. 19, consists of two adjacent parallel buried ridges, with one ridge operating as an optical receiver and the adjacent ridge operating as an optical transmitter. The receiving ridge consists of a semiconductor optical amplifier (SOA) and a photodetector for the amplification and detection of the input optical signal, respectively. The adjacent ridge consists of the same SG-DBR laser/EAM architecture as the transmitter.

In this photocurrent-driven wavelength converter, the detector and EAM electrodes are joined by a coplanar strip (CPS) interconnect. In this configuration, the photocurrent generated in the detector by the input optical signal will pass through a termination load, resulting in the small signal voltage swing across the EAM identical to that of the input data sequence. The EAM functions to write the data on the continuous wave output of the SG-DBR laser operating at any wavelength within the tuning band hence wavelength conversion is achieved.

The optical to optical frequency response of a wavelength converter with a 225 μm photodetector interconnected to a 175-μm modulator demonstrated a 3-dB bandwidth of over 12 GHz with a 25-Ω termination. To demonstrate 10-Gb/s operation, eye diagrams were taken for wavelength conversion from 1550 nm to 1555, 1562, 1569, and 1575 nm, as shown in Fig. 20. Although error-free operation was achieved, insufficient extinction ($\sim$2 dB) resulted in high power penalties ($\sim$8 dB). The insufficient extinction was a result of receiver inefficiencies such as inadequate photocurrent generation and saturation effects. These aspects of the device are being addressed with higher saturation power SOAs and photodetectors.

For example, higher extinction ratios and lower power penalties were observed in other wavelength-converter experiments, which used an offset quantum-well integration platform and higher saturation power SOAs and photodetectors in the receiver stage. One version used the integration of a slightly higher saturation power SOA-PIN receiver with an EAM-modulated SG-DBR to demonstrate 10-dB extinction and 2.5-dB power penalties back-to-back at 10 Gb/s over a wide tuning range [26]. A second wired a separate high-power SOA-PIN receiver with a MZ-modulated SG-DBR to demonstrate 12 dB of extinction, capable of positive and negative chirp, and 1.2 dB of power penalty at 10 Gb/s over 75 km of Corning SMF-28 fiber the 35-nm tuning range [27].

The QWI platform has also been used to fabricate monolithic tunable all-optical wavelength converters (TAO-WCs). These devices are among the most elaborate photonic integrated circuits fabricated to date in terms of the number of functional elements integrated into a single device. The devices, illustrated in Fig. 21, consist of a widely-tunable SG-DBR laser monolithically integrated with a semiconductor optical amplifier-based Mach-Zehnder Interferometer (MZI) wavelength converter. A schematic of the device is shown in Fig. 21.

The device works on the principle of optically induced index change in a SOA due to carrier density modulation. The cross phase modulation that results from the index change is then used

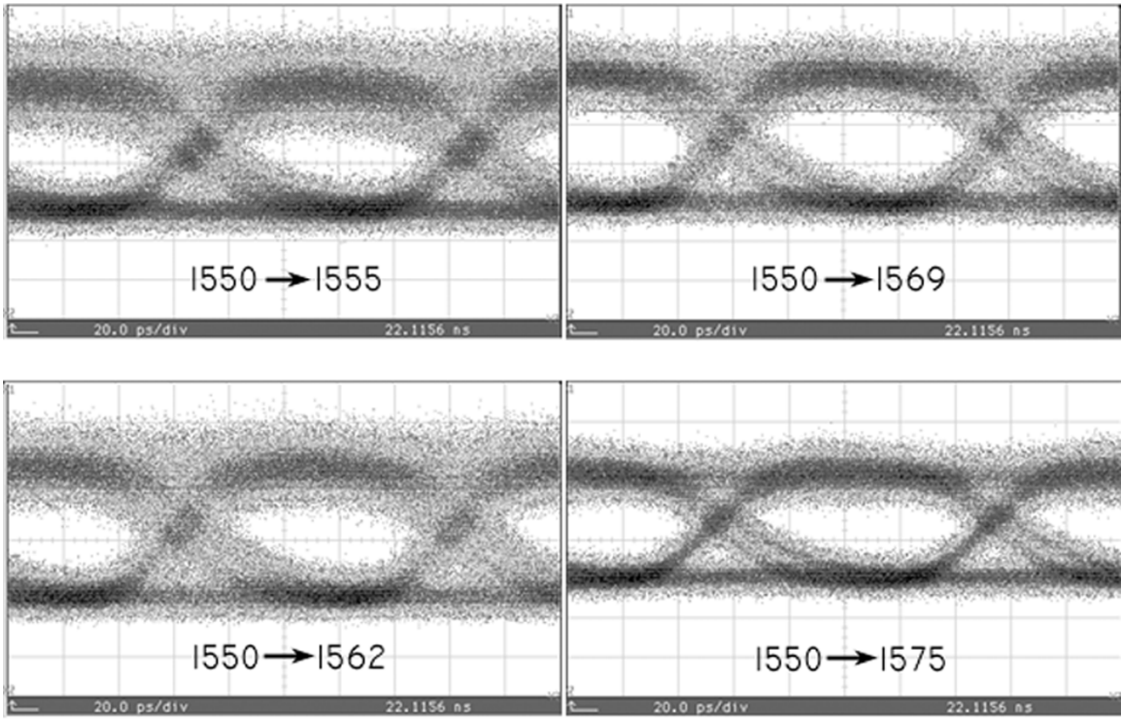

Fig. 20. The 10-Gb/s eye diagrams for wavelength conversion from 1550 to 1555 nm, 1562, 1569, and 1575 nm.

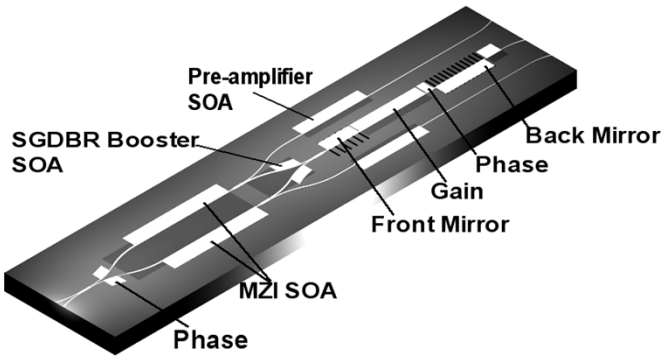

Fig. 21. QWI TAO-WC.

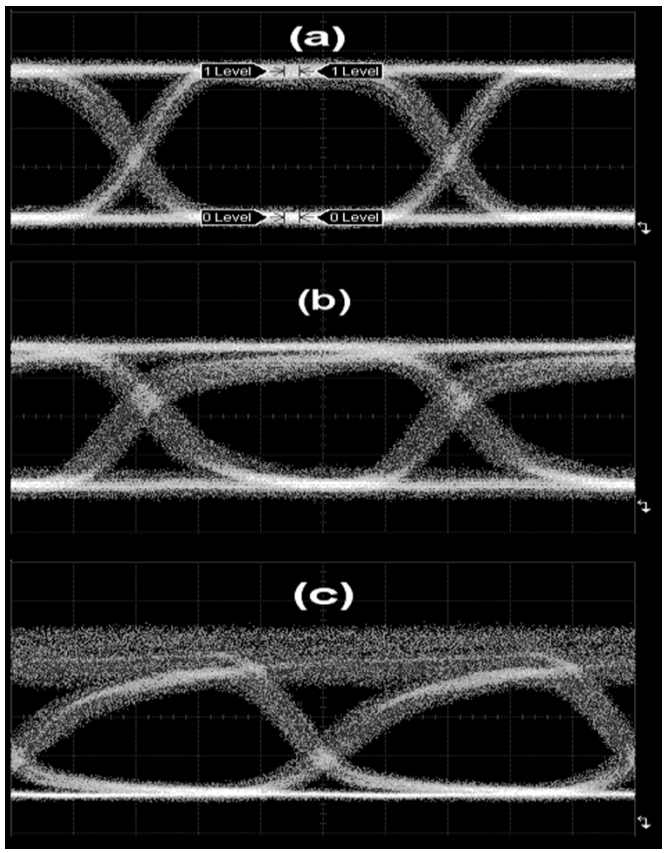

Fig. 22. (a) Input data to the device at 10 Gb/s. Wavelength converted data in the (b) noninverting and (c) inverting mode of operation.

to gate the SGDBR output using a MZI [29]–[31]. Fig. 22 shows the eye diagrams of the wavelength converted data in both the inverted and noninverted mode of operation. The current devices are capable of converting from any input wavelength to any output wavelength across the entire C-band (over 30-nm tuning range).

To maximize the speed of operation of this wavelength converter, it is important to reduce the carrier lifetimes in the SOA's in the MZI. This lifetime governed by the saturation properties and the material parameters of the SOA, i.e., carrier concentration, differential gain, the optical confinement factor, as well as the optical power in the SOA and the length of the SOA through the effects of high-pass filtering. Our earlier work on TAO-WCs [29]–[31] employed an offset quantum-well platform to fabricate the device, with inherent modal confinement factor of around 6%, which limited the minimum carrier lifetime attainable [30]. The QWI-based platform allows us to overcome this limitation and further reduce the carrier lifetime by using centered quantum wells with a significantly increased the confinement factor of over 9% in our current design. The value of the confinement factor can be tailored by the choice of the number of quantum wells.

Along with the benefit it offers, the increase in the confinement factor also creates additional challenges. The SOA saturation power reduction results in the enhancement of pattern dependence in the preamplifier SOAs. Optimizing the preamplifier designs in the QWI platform to get linear, high power amplification is a work in progress.

V. Conclusion

The development of photonic integrated circuits is key to the advancement of the fiber optic communications field. The introduction of new highly functional devices and systems must stem from innovation. This manuscript focused on the ability to monolithically integrate optoelectronic components through a novel QWI processing platform. Such a processing method allows for the optimization of the quantum well band edge for each integrated component. This allows designers to break many, but not all design tradeoffs in pursuit of high functionality photonic integrated circuits.

A QWI process has been developed which allows for the formation of multiple quantum-well band edges across the wafer. The use of an implant buffer layer not only prevented the implanted ions from damaging the quantum wells, but facilitated the development of a cyclic etch and anneal process enabling the strategic placement of the quantum well band edge for integrated devices.

There are an almost limitless number of applications for QWI in the development of high functionality photonic integrated circuits. The capability to monolithically integrate a number of devices each with a unique quantum-well band edge is an advancement that must be exploited. Although device improvement is certainly on the forefront of the QWI horizon, the real driving force for QWI applies to those devices and integration schemes that will be made possible in the future, and have yet to come.

References

[1] J. Binsma, P. Thijs, T. VanDongen, E. Jansen, A. Staring, G. VanDenHoven, and L. Tiemeijer, "Characterization of butt-joint InGaAsP waveguides and their application to 1310 nm DBR-Type MQW ganin-clamped semiconductor optical amplifiers," *IEICE Trans. Electron.*, vol. E80-C, pp. 675–681, 1997.

[2] M. Aoki, M. Suzuki, H. Sano, T. Kawano, T. Ido, T. Taniwatari, K. Uomi, and A. Takai, "InGaAs/InGaAsP MQW electroabsorption modulator integrated with a DFB laser fabricated by band-gap energy control selective area MOCVD," *IEEE J Quantum Electron.*, vol. 29, no. 6, pp. 2088–2096, Jun. 1993.

[3] B. Mason, G. Fish, S. DenBaars, and L. Coldren, "Ridge waveguide sampled grating DBR lasers with 22-nm quasi-continuous tuning range," *IEEE Photon. Technol. Lett.*, vol. 10, no. 9, pp. 1211–1213, Sep. 1998.

[4] S. McDougall, O. Kowalski, C. Hamilton, F. Camacho, B. Qiu, M. Ke, R. De La Rue, A. Bryce, and J. Marsh, "Monolithic integration via a universal damage enhanced quantum-well intermixing technique," *IEEE J. Sel. Topics Quantum Electron.*, vol. 4, no. 4, pp. 636–646, Jul./Aug. 1998.

[5] S. Charbonneau, E. Kotels, P. Poole, J. He, G. Aers, J. Haysom, M. Buchanan, Y. Feng, A. Delage, F. Yang, M. Davies, R. Goldberg, P. Piva, and I. Mitchell, "Photonic integrated circuits fabricated using ion implantation," *IEEE J. Sel. Topics Quantum Electron.*, vol. 4, no. 4, pp. 772–793, Jul./Aug. 1998.

[6] D. Hofstetter, B. Maisenholder, and H. Zappe, "Quantum-well intermixing for fabrication of lasers and photonic integrated circuits," *IEEE J. Sel. Topics Quantum Electron.*, vol. 4, no. 4, pp. 794–802, Jul./Aug. 1998.

[7] E. Skogen, J. Barton, S. DenBaars, and L. Coldren, "A quantum-well-intermixing process for wavelength-agile photonic integrated circuits," *IEEE J. Sel. Topics in Quantum Electron.*, vol. 8, no. 4, pp. 863–869, Jul./Aug. 2002.

[8] B. Mason, G. Fish, S. DenBaars, and L. Coldren, "Widely tunable sampled grating DBR lasers with integrated electroabsorption modulator," *IEEE Photon. Technol. Lett.*, vol. 11, no. 6, pp. 638–640, Jun. 1999.

[9] B. Mason, J. Barton, G. Fish, and L. Coldren, "Design of sampled grating DBR lasers with integrated semiconductor optical amplifiers," *IEEE Photon. Technol. Lett.*, vol. 12, no. 7, pp. 762–764, Jul. 2000.

[10] J. Barton, M. Mašanovic, E. Skogen, and L. Coldren, "Widely-tunable high-speed transmitters using integrated SGDBRs and Mach-Zehnder modulators," *IEEE J. Sel. Topics Quantum Electron.*, vol. 9, no. 5, pp. 1113–1117, Sep./Oct. 2003.

[11] D. Deppe and N. Holonyak, Jr., "Atom diffusion and impurity-induced layer disordering in quantum well III-V semiconductor heterostructures," *J. Appl. Phys.*, vol. 64, pp. 93–113, 1988.

[12] S. K. Si, D. H. Yeo, K. H. Yoon, and S. J. Kim, "Area selectivity of InGaAsP-InP multiquantum-well intermixing by impurity-free vacancy diffusion," *IEEE J. Sel. Topics Quantum Electron.*, vol. 4, no. 4, pp. 619–623, Jul./Aug. 1998.

[13] B. Qui, A. Bryce, R. De La Rue, and J. Marsh, "Monolithic integration in InGaAs-InGaAsP multiquantum-well structure using laser processing," *IEEE Photon. Technol. Lett.*, vol. 10, no. 6, pp. 769–771, Jun. 1998.

[14] S. Charbonneau, P. Poole, Y. Feng, G. Aers, M. Dion, M. Davies, R. Goldberg, and I. Mitchell, "Band-gap tuning of InGaAs/InGaAsP/InP laser using high energy ion implantation," *Appl. Phys. Lett.*, vol. 67, pp. 2954–2956, 1995.

[15] M. Paquette, J. Beauvais, J. Beerens, P. Poole, S. Charbonneau, C. Miner, and C. Blaauw, "Blueshifting of InGaAsP/InP laser diodes by low-energy ion implantation," *Appl. Phys. Lett.*, vol. 71, pp. 3749–3751, 1997.

[16] E. Skogen, J. Raring, J. Barton, S. DenBaars, and L. Coldren, "Post-growth control of the quantum-well band edge for the monolithic integration of widely-tunable lasers and electroabsorption modulators," *IEEE J. Sel. Topics Quantum Electron.*, vol. 9, no. 5, pp. 1183–1190, Sep./Oct. 2003.

[17] J. Shim, M. Yamaguchi, P. Delansay, and M. Kitamura, "Refractive index and loss changes produced by current injection in InGaAs(P)-InGaAsP Multiple Quantum-Well (MQW) waveguides," *IEEE J. Sel. Topics Quantum Electron.*, vol. 1, no. 2, pp. 408–415, Jun. 1995.

[18] H. Takeuchi, K. Tsuzki, K. Sato, M. Yamamoto, Y. Itaya, A. Sano, M. Yoneyama, and T. Otsuji, "Very high-speed light-source module up to 40 Gb/s containing an MQW electroabsorption modulator integrated with a DFB laser," *IEEE J. Sel. Topics Quantum Electron.*, vol. 3, pp. 336–343, Apr. 1997.

[19] H. Haisch, W. Baumert, C. Hache, E. Kühn, M. Klenk, K. Satzke, M. Schilling, J. Weber, and E. Zielinski, "10 Gbit/s standard fiber TDM transmission at 1.55 μm with low chirp monolithically integrated MQW electroabsorption modulator/DFB-laser realized by selective area MOVPE," in *Proc. 20th Eur. Conf. Optical Communication*, 1994, pp. 801–804.

[20] G. Morrison, E. Skogen, C. Wang, J. Raring, Y. Chang, M. Sysak, and L. Coldren, "Photocurrent spectroscopy for quantum-well intermixed photonic integrated circuit design," *IEEE Photon. Technol. Lett*, submitted for publication.

[21] E. Skogen, C. Wang, J. Raring, G. Morrison, and L. Coldren, "Small-footprint, high-efficiency, integrated transmitters for high-speed optical interconnect applications," presented at the *Proc. Integrated Photonics Research Conf.*, San Francisco, CA, June 30–July 2 2004, paper no. IThD2.

[22] C. Wang, E. Skogen, J. Raring, G. Morrison, and L. Coldren, "Short-cavity 1.55 μm DBR lasers integrated with high-speed EAM modulators," in *Proc. 19th Annu. IEEE Int. Semiconductor Laser Conf.*, Matsueshi, Simane, Japan, 2004.

[23] J. Raring, E. Skogen, L. Johansson, M. Sysak, J. Barton, M. Mašanović, and L. Coldren, "Demonstration of widely-tunable single-chip 10 GB/s laser-modulators using multiple-bandgap InGaAsP quantum-well intermixing," *IEEE Photon. Technol. Lett.*, vol. 16, no. 7, pp. 1613–1615, Jul. 2004.

[24] C. Henery, R. Logan, and K. Bertness, "Spectral dependence of the change in refractive index due to carrier injection in GaAs lasers," *J. Appl. Phys.*, vol. 52, no. 7, pp. 4457–4461, 1981.

[25] J. Fells, I. White, M. Gibbon, R. Penty, G. Thompson, A. Wright, R. Saunders, and C. Armistead, "Controlling the chirp in electroabsorption modulators under digital modulation," *Electron. Lett.*, vol. 30, no. 24, pp. 2066–2067, 1994.

[26] M. Sysak, J. Barton, J. Raring, M. Dummer, A. Tauke-Pedretti, D. Blumenthal, and L. Coldren, "10 Gb/s photocurrent driven, widely tunable electroabsorption modulator based wavelength converter," in *Proc. Optical Fiber Conf.*, 2005, submitted for publication.

[27] J. Barton, A. Tauke-Pedretti, M. Dummer, M. Sysak, M. Masanovic, J. Raring, E. Skogen, and L. Coldren, "10 Gbit/s wavelength conversion using a widely tunable series push-pull photocurrent-driven transmitter," *IEEE Photon. Technol. Lett.*, submitted for publication.
[28] V. Lal, M. Mašanović, E. Skogen, J. Summers, L. Coldren, and D. Blumenthal, "Widely tunable all-optical wavelength converter based on monolithic integration of a SGDBR and Mach-Zehnder interferometer using quantum well intermixing," IEEE Photon. Technol. Lett., submitted for publication.
[29] M. Mašanović, V. Lal, J. Barton, E. Skogen, L. Coldren, and D. Blumenthal, "Monolithically integrated Mach-Zehnder interferometer wavelength converter and widely-tunable laser in InP," *IEEE Photon. Technol. Lett.*, vol. 15, pp. 1117–1119, 2003, submitted for publication.
[30] M. L. Mašanović, V. Lal, J. A. Summers, J. S. Barton, E. J. Skogen, L. A. Coldren, and D. J. Blumenthal, "Design and performance of a monolithically-integrated widely-tunable all-optical wavelength converter with independent phase control," *IEEE Photonics Technology Letters*, vol. 16, no. 10, pp. 2299–2301, Oct. 2004.
[31] M. Mašanović, V. Lal, J. A. Summers, J. Barton, E. Skogen, L. Rau, L. Coldren, and D. Blumenthal, "Widely-tunable monolithically-integrated all-optical wavelength converters in InP," *IEEE J. Lightw. Technol.*, submitted for publication.

Erik J. Skogen received the B.S. degree from Iowa State University, Ames, in 1997, and the M.S. and Ph.D. degrees from the University of California at Santa Barbara (UCSB) in 1999 and 2003, respectively. His dissertation work involved the development and application of quantum-well intermixing techniques to widely-tunable sampled-grating DBR lasers and photonic integrated circuits (PICs).

He was a Postdoctoral Researcher with UCSB from 2003 to 2005, where he investigated advanced PICs. In 2005, he joined Sandia National Laboratories, Albuquerque, NM, as a Senior Member of the Technical Staff. His current research interests include monolithic integration techniques for next-generation PICs.

James W. Raring (S'02) was born in New Jersey in 1978. He received the B.S. degree from the Materials Engineering Department, California Polytechnic State University, San Luis Obispo, in 2001. He is currently working toward the Ph.D. degree in materials science from the University of California at Santa Barbara.

His research interests include the monolithic integration of widely tunable diode lasers into high-speed photonic integrated circuits with the use of quantum-well intermixing.

Gordon B. Morrison was born in Portsmouth, U.K., in 1973. He obtained his B.A.Sc. degree in engineering physics from Simon Fraser University, Vancouver, BC, Canada, in 1997, and the Ph.D. from the Department of Engineering Physics, McMaster University, Hamilton, ON, Canada, in 2002.

He is currently a Postdoctoral Researcher with the Department of Electrical and Computer Engineering, University of California at Santa Barbara (UCSB). His research interests at McMaster University included modeling the spectra of semiconductor lasers, fitting models to spectra for parameter extraction, and modeling gain in quantum well lasers. At UCSB, he has been involved in the design and characterization of integrated laser/modulator transmitters that are fabricated using quantum-well intermixing.

Chad S. Wang (S'99) was born in Racine, WI, in 1979. He received the B.S. degree from The University of Texas at Austin, in 2001, and the M.S. degree in 2002 from the University of California, Santa Barbara, where he is currently working toward the Ph.D. degree in electrical and computer engineering.

His research interests include the development of integrated laser-modulators for optical interconnect applications. He is also involved in molecular beam epitaxy growth of III-V semiconductor vertical cavity lasers and avalanche photodetectors.

Vikrant Lal received the B.S. degree in electrical engineering from the Indian Institute of Technology, Delhi, India, 1999, and the M.S. degree majoring in communications engineering in electrical and computer engineering from the University of Maryland, College Park, in 2001. He is currently working toward the Ph.D. degree student in electrical and computer engineering at the University of California at Santa Barbara.

His research interests include photonic integrated circuits and all-optical switching.

Milan L. Mašanović graduated as a valedictorian from the School of Electrical Engineering, University of Belgrade, Belgrade, Yugoslavia, in 1998. He received the M.S. degree and Ph.D. degree in electrical engineering from the Department of Electrical and Computer Engineering, University of California at Santa Barbara in 2000 and 2004, respectively.

His research interests include InP photonic integrated circuits with emphasis on integrated tunable wavelength converters and their applications in novel all-optical networks.

Dr. Mašanović is the winner of numerous awards and fellowships including the 2004 IEEE-Laser and Electro-Optics Society Graduate Student Fellowship Award and the 2003 Best Student Paper Award at the Indium Phosphide and Related Materials Conference.

Larry A. Coldren (S'67–M'72–SM'77–F'82) received the Ph.D. degree in electrical engineering from Stanford University, Stanford, CA, in 1972.

After 13 years in the research area at Bell Laboratories, he was appointed Professor of Electrical and Computer Engineering at the University of California at Santa Barbara (UCSB) in 1984. In 1986, he assumed a joint appointment with Materials and ECE, and in 2000, the Fred Kavli Chair in Optoelectronics and Sensors. He is also Chairman and Chief Technology Officer of Agility Communications, Inc. At UCSB, his efforts have included work on novel guided-wave and vertical-cavity modulators and lasers, as well as the underlying materials growth and fabrication technology. He is now investigating the integration of various optoelectronic devices, including optical amplifiers and modulators, tunable lasers, wavelength-converters, and surface-emitting lasers. He has authored or coauthored over 500 papers, five book chapters, one textbook, and has been issued 32 patents.

Dr. Coldren is a past Vice-President of the IEEE Lasers and Electro-Optics Society and a Fellow of the Optical Society of America.